Wireless Networks and Mobile Communications Series

MILLIMETER WAVE TECHNOLOGY IN WIRELESS PAN, LAN, AND MAN

Edited by
Shao-Qiu Xiao
Ming-Tuo Zhou
Yan Zhang

CRC Press
Taylor & Francis Group
AN AUERBACH BOOK

MILLIMETER WAVE TECHNOLOGY IN WIRELESS PAN, LAN, AND MAN

WIRELESS NETWORKS AND MOBILE COMMUNICATIONS

Dr. Yan Zhang, Series Editor
Simula Research Laboratory, Norway
E-mail: yanzhang@ieee.org

Unlicensed Mobile Access Technology: Protocols, Architectures, Security, Standards and Applications
Yan Zhang, Laurence T. Yang and Jianhua Ma
ISBN: 1-4200-5537-2

Wireless Quality-of-Service: Techniques, Standards and Applications
Maode Ma, Mieso K. Denko and Yan Zhang
ISBN: 1-4200-5130-X

Broadband Mobile Multimedia: Techniques and Applications
Yan Zhang, Shiwen Mao, Laurence T. Yang and Thomas M Chen
ISBN: 1-4200-5184-9

The Internet of Things: From RFID to the Next-Generation Pervasive Networked Systems
Lu Yan, Yan Zhang, Laurence T. Yang and Huansheng Ning
ISBN: 1-4200-5281-0

Millimeter Wave Technology in Wireless PAN, LAN, and MAN
Shao-Qiu Xiao, Ming-Tuo Zhou and Yan Zhang
ISBN: 0-8493-8227-0

Security in Wireless Mesh Networks
Yan Zhang, Jun Zheng and Honglin Hu
ISBN: 0-8493-8250-5

Resource, Mobility and Security Management in Wireless Networks and Mobile Communications
Yan Zhang, Honglin Hu, and Masayuki Fujise
ISBN: 0-8493-8036-7

Wireless Mesh Networking: Architectures, Protocols and Standards
Yan Zhang, Jijun Luo and Honglin Hu
ISBN: 0-8493-7399-9

Mobile WIMAX: Toward Broadband Wireless Metropolitan Area Networks
Yan Zhang and Hsiao-Hwa Chen
ISBN: 0-8493-2624-9

Distributed Antenna Systems: Open Architecture for Future Wireless Communications
Honglin Hu, Yan Zhang and Jijun Luo
ISBN: 1-4200-4288-2

MILLIMETER WAVE TECHNOLOGY IN WIRELESS PAN, LAN, AND MAN

Edited by
Shao-Qiu Xiao
Ming-Tuo Zhou
Yan Zhang

CRC Press
Taylor & Francis Group
Boca Raton London New York

CRC Press is an imprint of the
Taylor & Francis Group, an **informa** business
AN AUERBACH BOOK

Auerbach Publications
Taylor & Francis Group
6000 Broken Sound Parkway NW, Suite 300
Boca Raton, FL 33487-2742

Printed in the United States of America on acid-free paper
10 9 8 7 6 5 4 3 2 1

International Standard Book Number-13: 978-0-8493-8227-7 (Hardcover)

Library of Congress Cataloging-in-Publication Data

Xiao, Shao-Qiu.
Millimeter wave technology in wireless Pan, Lan, and Man / Shao-Qiu Xiao, Ming-Tuo Zhou, and Yan Zhang.
p. cm.
Includes bibliographical references and index.
ISBN-13: 978-0-8493-8227-7 (alk. paper) 1. Broadband communication systems. 2. Wireless communication systems. 3. Millimeter waves. I. Zhou, Ming-Tuo. II. Zhang, Yan, 1977- III. Title.

TK5103.4.X53 2007
004.6'8--dc22 2007011241

Visit the Taylor & Francis Web site at
http://www.taylorandfrancis.com

and the Auerbach Web site at
http://www.auerbach-publications.com

Contents

List of Contributors

Dan An
Millimeter-wave INnovation Technology Research Center
Department of Electronic Engineering
Dongguk University
Seoul, Korea

Pantel D. M. Arapoglou
National Technical University of Athens
Athens, Greece

T. Chen
CREATE-NET International Research Center
Trento, Italy

I. Chlamtac
CREATE-NET International Research Center
Trento, Italy

Panayotis G. Cottis
National Technical University of Athens
Athens, Greece

X. James Dong
University of California
Berkeley, California

James P. K. Gilb
SiBEAM
Fremont, California

Joerg Habetha
Philips Research Laboratories
Aachen, Germany

Sung-Chan Kim
Millimeter-wave INnovation Technology Research Center
Department of Electronic Engineering
Dongguk University
Seoul, Korea

Andrey Kobyakov
Corning Inc.
Corning, New York

J. Laskar
Georgia Institute of Technology
Atlanta, Georgia

Bok-Hyung Lee
Millimeter-wave INnovation Technology Research Center
Department of Electronic Engineering
Dongguk University
Seoul, Korea

J.-H. Lee
Georgia Institute of Technology
Atlanta, Georgia

Sheung L. Li
SiBEAM
Fremont, California

Huilai Liu
University of Electronics Science and Technology of China
Chengdu, China

Jim Misener
University of California
Berkeley, California

John Mitchell
University College London
London, U.K.

Athanasios D. Panagopoulos
National Technical University of Athens
Athens, Greece

Javier del Pardo
Philips Semiconductors
Sophia Antipolis, France

S. Pinel
Georgia Institute of Technology
Atlanta, Georgia

Emma Regentova
University of Nevada
Las Vegas, Nevada

Jin-Koo Rhee
Millimeter-wave INnovation Technology Research Center
Department of Electronic Engineering
Dongguk University
Seoul, Korea

Michael Sauer
Corning Inc.
Corning, New York

M. M. Tentzeris
Georgia Institute of Technology
Atlanta, Georgia

Pravin Varaiya
University of California
Berkeley, California

Bing-Zhong Wang
University of Electronics Science and Technology of China
Chengdu, China

Jianpeng Wang
University of Electronics, Science and Technology of China
Chengdu, China

H. Woesner
CREATE-NET International Research Center
Trento, Italy

Shao-Qiu Xiao
University of Electronics, Science and Technology of China
Chengdu, China

Felix Yanovsky
The National Aviation University
Kiev, Ukraine

Jijun Yao
National University of Singapore
Singapore

Wenbing Zhang
University of California
Berkeley, California

Yan Zhang
Simula Research Laboratory
Lysaker, Norway

Jun Zheng
Queens College
City University of New York
New York, New York

Ming-Tuo Zhou
National Institute of Information
and Communications Technology
Singapore

Chapter 1

Millimeter-Wave Monolithic Integrated Circuit for Wireless LAN

Jin-Koo Rhee, Dan An, Sung-Chan Kim, and Bok-Hyung Lee

Contents

1.1 Introduction

The increase in high-performance personal computers (PCs) and multimedia equipment in offices and homes requires high-speed and broadband wireless data transmission. This requirement makes wireless indoor communication systems such as wireless local area networks (WLAN) and personal area networks (PAN) because of their portable convenience. For such short-range indoor broadband WLAN and PAN systems, the millimeter-wave band offers significant advantages in supplying enough bandwidth for the transmission of various multimedia content. In particular, there has been an increasing requirement for the development of the V-band WLAN for commercial applications. The frequency of 60 GHz is very useful for short-distance wireless communications due to the strong absorption characteristic by oxygen in the atmosphere. Therefore, frequency efficiency is improved compared to other frequency bands. In the last few decades, many research groups in the world have developed millimeter-wave LAN systems. For example, Communications Research Laboratory (CRL, now NiCT) took up the project of developing indoor WLAN systems using millimeter waves in 1992 [1]. The final goal of the millimeter-wave WLAN systems is to provide point-to-multipoint access with transmission rates higher than 100 Mbps for the connectivity of broadband integrated services digital networks (B-ISDNs) or conventional fast Ethernet. For these millimeter-wave WLAN applications, we have to solve some problems. First of all, we have to reduce the size and cost of the systems. The millimeter-wave systems are generally fabricated using HIC (hybrid integrated circuit) technology, causing a large system. MMIC (monolithic millimeter-wave integrated circuit) technology is regarded as an alternative to HIC technology due to its ability to integrate active with passive elements on a single semiconductor substrate [2–6]. The MMIC has advantages, such as small size, high reliability, high productivity, and low cost due to using semiconductor technologies compared to the conventional HIC. The main objective of this chapter is to discuss the MMIC technology and its applications for millimeter-wave wireless LAN. First, millimeter-wave WLAN will be introduced. Then, the modeling of active and passive devices will be described. The design and fabrication technologies of millimeter-wave circuits are presented. Finally, millimeter-wave monolithic circuits for WLAN applications are explained.

1.2 Millimeter-Wave Wireless Local Area Network

Recently, a broadband and high-speed indoor network for office and home environments has been required. Additionally, microwave frequency bands have been saturated and there is growing necessity to exploit new frequency bands that have not yet been utilized for commercial applications. For this reason, utilization of the millimeter-wave band has been recommended, and much research has been devoted to developing millimeter-wave wireless LAN. Advantages of millimeter-wave communication are very wide frequency band, high-speed transmission, and radiated power limitation for unlicensed use. Therefore, millimeter-wave WLAN can be utilized in short-range communication and indoor networks. In particular, a 60-GHz band is very useful for wireless short-distance communications due to strong absorption by oxygen. Thus, compared to other frequency bands, frequency efficiency is improved. Figure 1.1 shows the atmospheric absorption versus frequency [7]. Features to be noted are:

1. Good coexistence between millimeter-wave system and 802.11a/b/g & Bluetooth due to large frequency difference
2. Higher speed transmission, more than 1 Gbps
3. Exploitation of antenna directivity
4. Simple modulation/demodulation
5. Simple signal processing

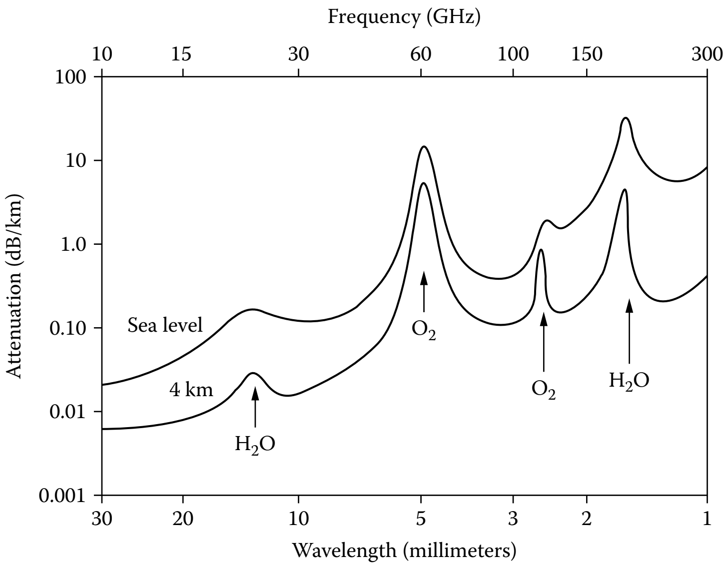

Figure 1.1 Average atmospheric absorption of frequency.

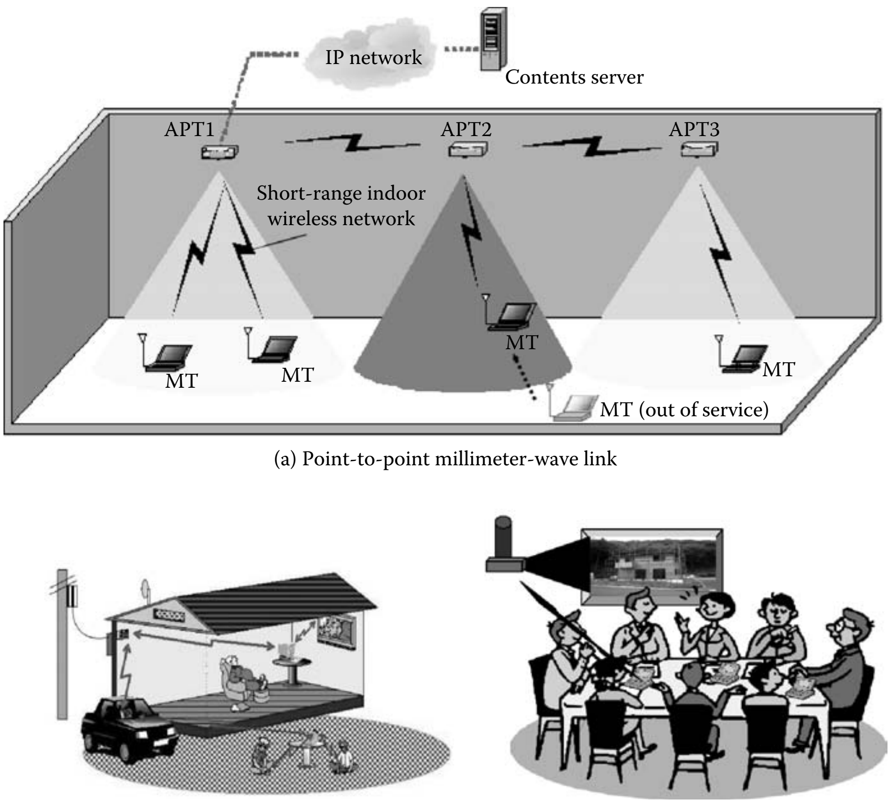

(a) Point-to-point millimeter-wave link

(b) Home utilization

(c) Office utilization

Figure 1.2 Utilizations of millimeter-wave wireless LAN.

Millimeter-wave WLAN is possible for wireless networks such as multimedia equipment, home appliances, videosignal transmissions, and personal computers. Utilization of millimeter-wave WLAN is explained in Figure 1.2. A millimeter-wave circuit and system have been developed using a waveguide module, hybrid integrated circuit method, resulting in large size, high cost, and low productivity. Use of these systems in wireless LAN has many problems due to small size and low cost in wireless LAN. To overcome these problems, high-speed devices such as high electron mobility transistors (HEMTs) and MMTCs need to be added to the millimeter-wave wireless LAN. Figure 1.3 shows normal millimeter-wave WLAN and millimeter-wave circuit components. Millimeter-wave components are usually composed of a low-noise amplifier (LNA), a power amplifier, an oscillator, and an up/down mixer. Also, passive components such as a filter, an antenna, a coupler, and a circulator are required. These components can be varied with system architecture. Millimeter-wave circuits must be

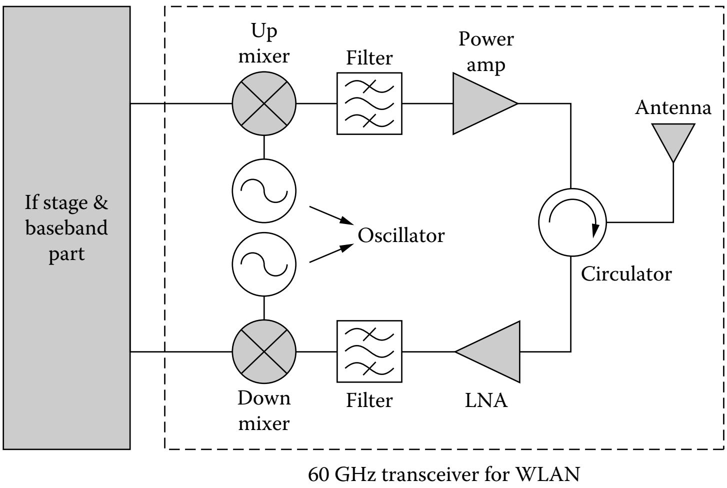

Figure 1.3 Millimeter-wave WLAN and millimeter-wave circuit components (IF, intermediate frequency).

realized high-speed operating characteristics, high linearity, small size, and low cost. For this reason, many technologies such as device modeling, circuit design, circuit fabrication, and measurement technology need to be developed for MMICs.

1.3 Millimeter-Wave Monolithic Integrated Circuit Technology

1.3.1 Millimeter-Wave Device and Modeling

1.3.1.1 Millimeter-Wave HEMT Technology

To fabricate the MMIC devices for the 60-GHz wireless LAN system, the development of active devices that have a high frequency, low noise, and high power performance is an essential theme. Since introduced in 1981 [8], the AlGaAs/GaAs HEMT has been widely used for the microwave region hybrid and monolithic circuits. However, the frequency performances of the conventional AlGaAs/GaAs HEMT devices cannot satisfy the millimeter-wave region (30–300 GHz) MMIC applications. In order to obtain the high-frequency performance, a Pseudomorphic HEMT (PHEMT), which has a relatively low energy band gap characteristic for higher conduction band offset, has been developed. The PHEMT epitaxial structure is shown in Figure 1.4. The epitaxial structure of the device consists of the following layers: an 500 nm GaAs buffer layer, an 18.5/1.5 nm AlGaAs/GaAs × 10 super-lattice buffer layer, a silicon planar doped layer ($1\times10^{12}/cm^2$), a 6-nm

GaAs capping layer, $5 \times 10^{18}/cm^3$, 30 nm
AIGaAs donor layer, undoped, 25 nm
δ-doping layer, $5 \times 10^{12}/cm^2$
AIGaAs spacer layer, undoped, 4.5 nm
AIGaAs channel layer, undoped, 12 nm
AIGaAs spacer layer, undoped, 6 nm
δ-doping layer, $1 \times 10^{12}/cm^2$
GaAs super lattice buffer, 500 nm
Semi-insulating GaAs substrate

Figure 1.4 The epitaxial structure for PHEMT fabrication. (Copyright 2004. With permission from Elsevier.)

AlGaAs lower spacer layer, a 12-nm InGaAs channel layer, a 4-nm AlGaAs upper spacer layer, a silicon planar doped layer ($5 \times 10^{12}/cm^2$), a 25-nm AlGaAs donor layer, and a 30-nm GaAs cap layer [9–10]. In this chapter, the DC characteristics of the 70 μm $\times$ 2 PHEMTs were measured by an HP 4156A DC parameter analyzer. The obtained DC performances show a knee voltage (Vk) of 0.6 V, a pinch-off voltage (Vp) of –1.5 V, a drain-source saturation current (Idss) density of 384 mA/mm and a maximum extrinsic transconductance of 367.9 mS/mm, as shown in Figure 1.5. Radio frequency (RF) characteristics of the PHEMTs were examined by an HP 8510C vector network analyzer. The measurement of S-parameters was performed in a frequency range of 1–50 GHz. For this RF measurement, the drain and gate bias conditions of 2 V and –0.6 V were used. We obtained a current gain cut-off frequency (ft) of 113 GHz, a maximum frequency of oscillation (fmax) of 180 GHz, and a measured S21 gain of 3.9 dB at 50 GHz, as shown in Figure 1.6. HEMTs on InP substrates have demonstrated superior microwave and low-noise performances compared to PHEMTs on GaAs substrates. The excellent device performances of the InP-based HEMTs operating in the millimeter-wave region is mostly based on the InGaAs/InAlAs/InP material system. However, compared to GaAs-based wafers, InP-based wafers have some critical drawbacks, such as the mechanical fragility of the wafers and the higher material cost. Moreover, InP-based HEMTs are not quite proper for large-scale production because the backside etching rate for the InP material is much slower. In recent decades, active research has been done on GaAs-based metamorphic HEMTs (MHEMTs) to address the needs for both high microwave performance and low device cost [11–13]. The use of metamorphic buffers on GaAs substrates was introduced to accommodate the lattice mismatch between the substrate and the active layers, as

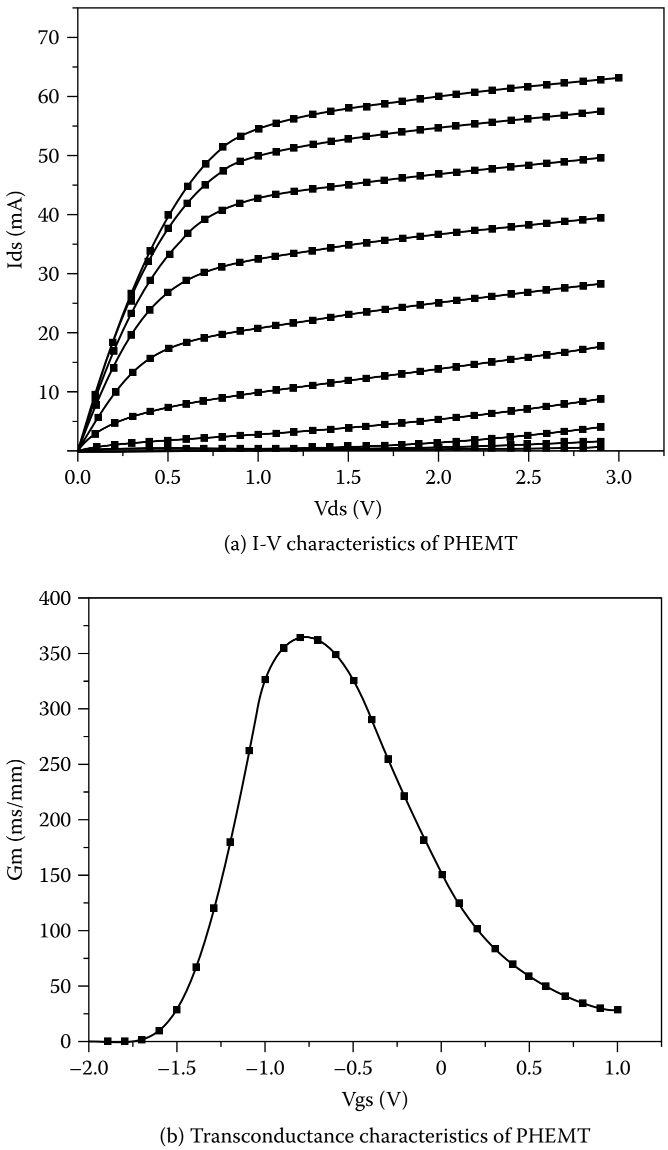

Figure 1.5 DC characteristics of GaAs pseudomorphic HEMT (gate length: 0.1 μm, total gate width: 140 μm). (Copyright 2004. With permission from Elsevier.)

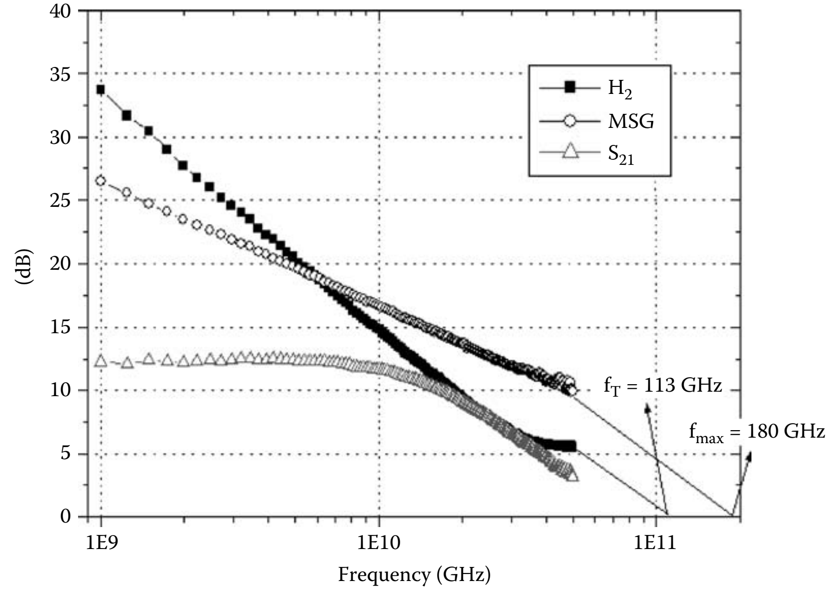

Figure 1.6 The RF characteristics of pseudomorphic HEMT (gate length: 0.1 μm, total gate width: 140 μm). (Copyright 2004. With permission from Elsevier.)

well as to avoid the InP substrates. By using the metamorphic buffers, unstrained InGaAs/InAlAs hetero-structures could be grown over a wide range of indium (In) contents for the InGaAs channels, thereby exhibiting device performances comparable to those of InP-based HEMTs. In Figure 1.7, the device active layers of MHEMT are grown on a strain-relaxed, compositionally graded, metamorphic buffer layer. The buffer layer provides the ability to adjust the lattice constant to any indium content channel desired, and therefore allows the device designer an additional degree of freedom to optimize the transistors for high frequency gain, power, linearity, and low noise and to trap dislocations and prevent them from propagating into the device channel. The DC and transfer characteristics of the MHEMT were measured using an HP 4156A semiconductor parameter analyzer. As shown in Figure 1.8, a pinch-off voltage of –1.5 V and a drain saturation current of 96 mA were measured at a gate voltage (Vgs) of 0 V. The fabricated MHEMT also showed a maximum transconductance of 760 mS/mm at a Vgs of –0.3 V and a drain voltage (Vds) of 1.8 V. The S-parameters of the MHEMTs were measured using an ME7808A Vector Network Analyzer in a frequency range from 0.04 to 110 GHz. In Figure 1.9, we showed the measured S21, h21, and maximum stable gain (MSG) of the MHEMT. The measured S21, ft, and fmax of the MHEMT were 6 dB (at 110 GHz), 195 GHz, and 391 GHz, respectively.

InGaAs capping layer, $6 \times 10^{18}/cm^3$, 15 nm
InAIAs donor layer, undoped, 15 nm
δ-doping layer, $4.5 \times 10^{12}/cm^2$
InAIAs spacer layer, undoped, 3 nm
InGaAs channel layer, undoped, 23 nm
InAIAs spacer layer, undoped, 4 nm
δ-doping layer, $1.3 \times 10^{12}/cm^2$
InAIAs buffer layer, undoped, 400 nm
$In_xAI_{1-x}As$ (x = 0~0.5) Metamorphic buffer, undoped, 1000 nm
Semi-insulating GaAs substrate

Figure 1.7 The epitaxial structure for MHEMT fabrication.

1.3.1.2 Millimeter-Wave Active Device Modeling

A small-signal equivalent model is widely used to analyze the characteristics of gains and noises of active devices. These models provide a vital connection between measured S-parameters and the electrical operating characteristics of the device. A more precise small-signal model provides some of the most important information in designing the devices and circuits as well. The components in the small-signal equivalent circuit are composed of a lumped element approximation to some aspect of the device physics. The small-signal equivalent model consists of both extrinsic and intrinsic elements. In general, the operating characteristics of devices may be mainly decided by the intrinsic elements such as Cgs, Cgd, Cds, gm, gds, and Ri. The values of intrinsic elements may be varied by the values of extrinsic elements. Therefore, through the precise extraction of the values of extrinsic elements, a more precise small-signal equivalent model may be formed. The small-signal parameter extraction of the HEMT is very useful for the device modeling and analysis in the design of millimeter-wave circuits. The small-signal equivalent circuit of an HEMT is shown in Figure 1.10. Basically, this equivalent circuit can be divided into two parts: (1) the intrinsic elements gm, Rds, Cgs, Cgd, Cds, Ri, and which are functions of the biasing conditions; and (2) the extrinsic elements Lg, Ld, Ls, Rg, Rd, Rs, Cpg, and Cpd, which are independent of the biasing conditions.

The extraction method of small-signal parameters has usually used the Dambrine method [14]. Figure 1.11 and Table 1.1 show the procedure of small-signal extraction and the extracted small-signal parameters of normal GaAs HEMTs, respectively. A small-signal model depicts linear characteristics of the device, while a large-signal model expresses nonlinear

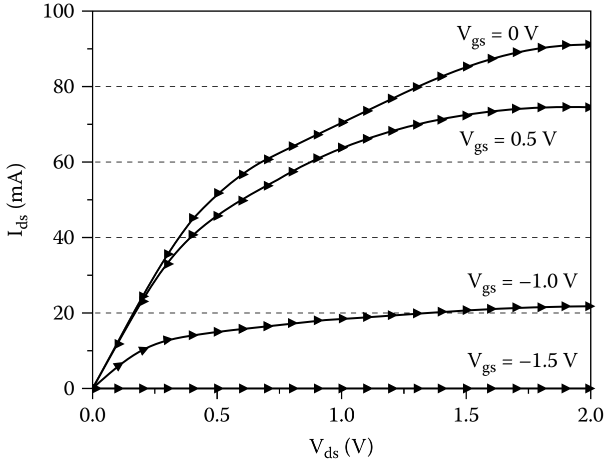

(a) I-V characteristics of MHEMT

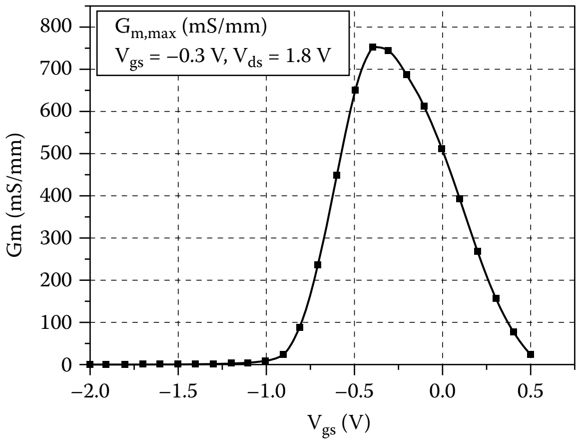

(b) Transconductance characteristics of MHEMT

Figure 1.8 DC characteristics of GaAs metamorphic HEMT (gate length: 0.1 μm, total gate width: 140 μm).

characteristics of the device. Analytical large-signal models approximate the nonlinear properties of an active device using a unique set of analytical equations. These nonlinear characteristics can be related to elements of the large-signal equivalent circuit. The large-signal parameters and the equivalent circuit are shown in Table 1.2 and Figure 1.12 respectively [15]. The large-signal model of the device can be used to analyze the performance of the nonlinear components, such as a power amplifier, an oscillator, a mixer, etc. Several studies have developed a large-signal model that

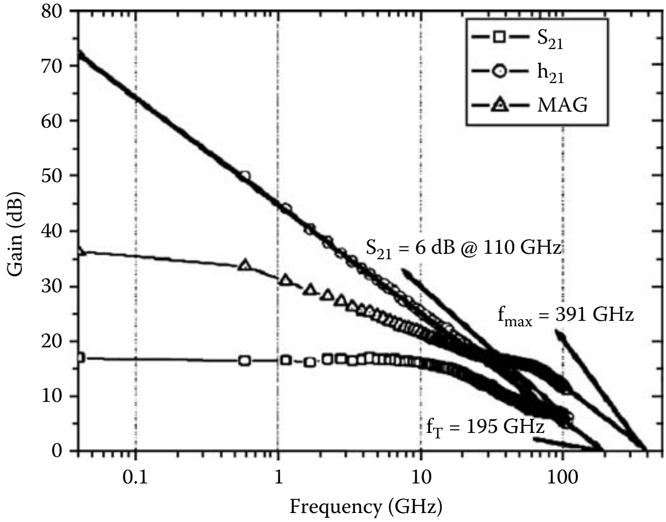

Figure 1.9 The RF characteristics of metamorphic HEMT (gate length: 0.1 μm, total gate width: 140 μm).

describes the nonlinear characteristics of a device. These models include the Curtice model, Statz model, TriQuint Own Model (TOM), Root, etc. The large-signal modeling method is generally following procedures and is shown in Figure 1.13: (1) device measurement (DC, RF characteristics), (2) extraction of parameter set using analytical equations, (3) a simulation

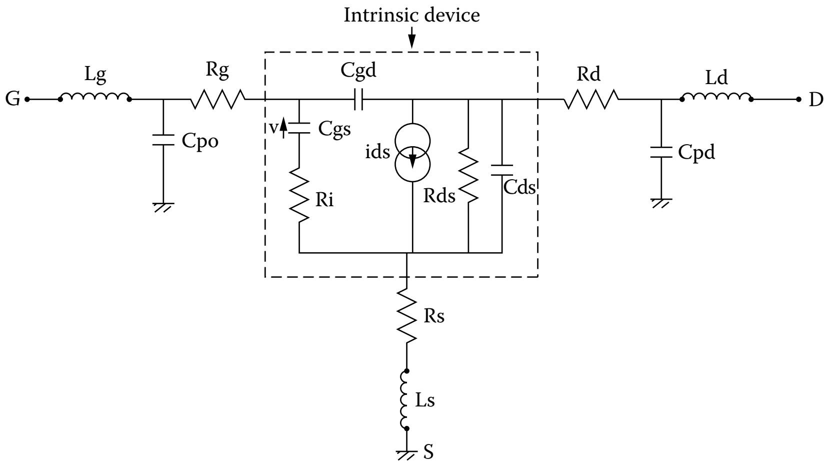

Figure 1.10 A small-signal equivalent circuit of HEMT.

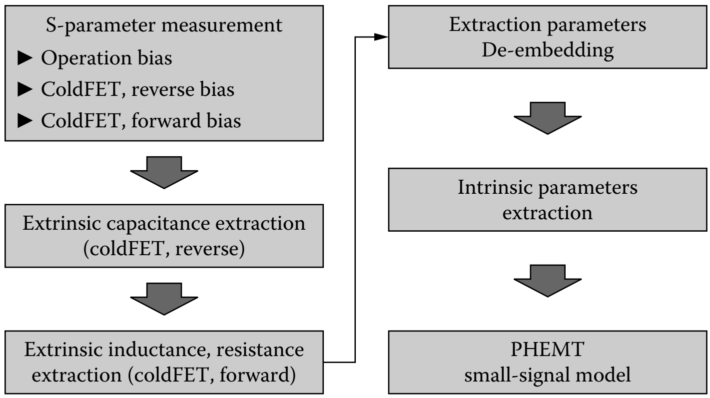

Figure 1.11 The procedure of small-signal modeling.

Table 1.1 The Extracted Small-Signal Parameters of GaAs, PHEMTs, and MHEMTs (gate length: 0.1 μm; total gate width: 140 μm)

Extrinsic Parameter	*Value*	*Intrinsic Parameter*	*Value*
(a) GaAs Pseudomorphic HEMT			
R_g [Ω]	1.980	C_{gs} [pF]	0.178
R_d [Ω]	6.900	C_{gd} [pF]	0.010
R_s [Ω]	3.120	C_{ds} [pF]	0.012
L_g [nH]	0.085	R_{ds} [Ω]	782.2
L_d [nH]	0.140	G_m [mS]	58.59
L_s [nH]	0.011	τ [psec]	1.190
C_{pg} [pF[	0.060	R_i [Ω]	2.310
C_{pd} [pF]	0.040		
(b) GaAs Metamorphic HEMT			
R_g [Ω]	2.560	C_{gs} [pF]	0.062
R_d [Ω]	6.730	C_{gd} [pF]	0.005
R_s [Ω]	2.600	C_{ds} [pF]	0.003
L_g [nH]	0.210	R_{ds} [Ω]	1143
L_d [nH]	0.094	G_m [mS]	83.73
L_s [nH]	0.006	τ [psec]	1.030
C_{pg} [pF[	0.054	R_i [Ω]	1.720
C_{pd} [pF]	0.052		

Table 1.2 The Large-Signal Parameters of GaAs PHEMTs and MHEMTs (gate length: 0.1 μm; total gate width: 140 μm; EEHEMT1 model)

Parameter	*Description*	*PHEMT (Unit)*	*MHEMT (Unit)*
Vto	Zero-bias threshold parameter	−1.679 (V)	−1.237 (V)
Vgo	Gate-source voltage where transconductance is maximum	−634.2 (mV)	−687.0 (mV)
Gm, max	Peak transconductance parameter	46.83 (mS)	76.21 (mS)
Vsat	Drain-source current saturation parameter	973.0 (mV)	193.2.0 (mV)
Kappa	Output conductance parameter	0.013 (1/V)	0.025 (1/V)
C11o	Maximum input capacitance for Vds = Vdso and Vdso > Deltds	129.2 (fF)	72.4(fF)
C11th	Minimum input capacitance for Vds = Vdso	184.9 (aF)	67.57 (aF)
Vinfl	Inflection point in C11-Vgs characteristic	−1.120 (V)	−1.958 (V)
Deltgs	C11th to C11o transition voltage	11.831 (V)	12.071 (V)
Deltds	Linear region to saturation region transition parameter	1.103 (V)	0.160 (V)
Lambda	C11-Vds characteristics slope parameter	0.348 (1/V)	0.696 (1/V)
C12sat	Input transcapacitance for Vgs = Vinfl and Vds > Deltds	20.46 (fF)	5.934 (fF)
Cgdsat	Gate-drain capacitance for Vds >Deltds	15.40 (fF)	21.77(fF)
Cdso	Drain-source inter-electrode capacitance	15.20 (fF)	20.48 (aF)
Rdb	Dispersion source output impedance	1,000 (Gohms)	1.300 (Gohms)
Cds	Dispersion source capacitance	160.0 (fF)	183.0 (fF)
Gdbm	Additional d—b branch conductance at Vds = Vdsm	51.31 (uS)	50.87 (uS)
Gmmaxac	Peak transconductance parameter (AC)	42.57 (mS)	63.81 (mS)
Vtoac	Zero-bias threshold parameter (AC)	−1.703 (V)	−2.376 (V)
Gammaac	Vds-dependent threshold parameter (AC)	35.14 (mS)	43.63 (mS)
Kappaac	Output conductance parameter (AC)	65.13u (1/V)	67.25u (1/V)
Peffac	Channel-to-backside self-heating parameter (AC)	15.75 (W)	29.56 (W)
Vco	Voltage where transconductance compression begins	−660.2 (mV)	−1.071 (mV)
Mu	Parameter that adds Vds dependence to transconductance compression	0.0024 (dimensionless)	0.0043 (dimensionless)
Vba	Transconductance compression “tail-off” parameter	1.001 (V)	1.331 (V)
Vbc	Transconductance roll-off to tail-off transition voltage	701.4 (mV)	849.8 (mV)
Deltgm	Slope of transconductance compression characteristic	267.2 (mS/V)	51.11 (mS/V)
Alpha	Transconductance saturation-to-compression transition parameter	2.094 (V)	1.033 (V)

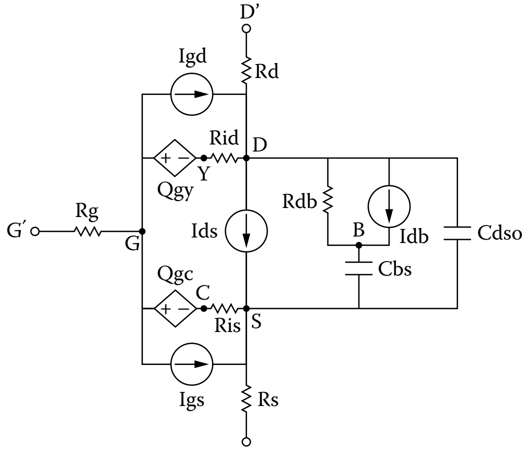

Figure 1.12 The equivalent circuit of an HEMT large-signal model (EEHEMT1 model).

using extracted parameter, (4) a comparison of measured characteristics and simulated characteristics, (5) an optimization of nonlinear. Figure 1.14 shows the comparison of measured and simulated results of a large-signal model (0.1 GaAs MHEMT) in frequency range from 1 to 110 GHz at the gate voltage of –1.0 V and the drain voltage of 1.8 V.

1.3.1.3 Millimeter-Wave Passive Device Modeling

In MMIC design, passive components are used for impedance matching, DC biasing, phase-shifting, and many other functions. These elements include not only the distributed transmission lines such as a coplanar waveguide

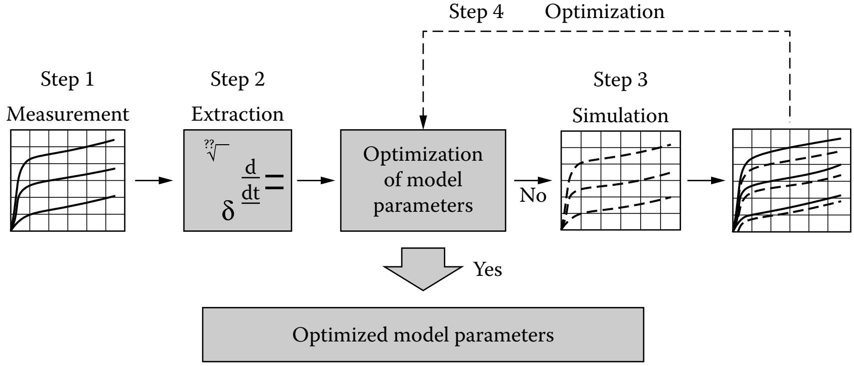

Figure 1.13 The procedure of nonlinear large-signal modeling.

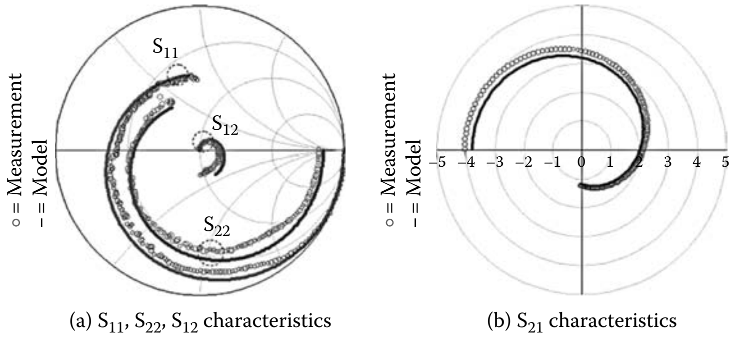

Figure 1.14 The modeling result of GaAs MHEMT (gate length: 0.1 μm; total gate width: 140 μm, gate voltage: –1.0 V; drain voltage: 1.8 V; —: model; o: measurement; frequency range: 1 $\sim$ 110 GHz).

(CPW) and a microstrip line but also the lumped capacitors and resistors. In millimeter-wave range, the distributed transmission lines have been mainly used because of low resonance frequency of lumped elements. In this chapter, the CPW structure was employed, because it has many advantages over the microstrip line structure in millimeter wave. It is well known that CPW-based MMIC processes may be cheaper than microstrip-based processes with holes and have high yield because backside processes are not needed [16–20]. Furthermore, CPW structure increases the packing density of the circuit and reduces the substrate dispersion characteristics for millimeter-wave operation. Figure 1.15 shows the CPW structure on GaAs substrate. The CPW models include curves, T junctions, and cross junctions as well as common elements, as shown in Figure 1.16. For simulation of the designed CPW, we used commercial software such as LineCalc of ADS from Agilent Incorporated. Figure 1.17 explains the extraction technology of passive device modeling. The passive libraries were finally completed after optimization by comparing the measured S-parameters with the momentum-simulated S-parameters. Metal–insulator–metal (MIM) capacitors and the

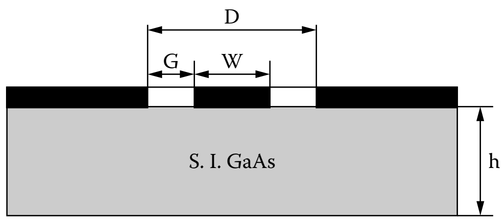

Figure 1.15 The coplanar waveguide (CPW) structure.

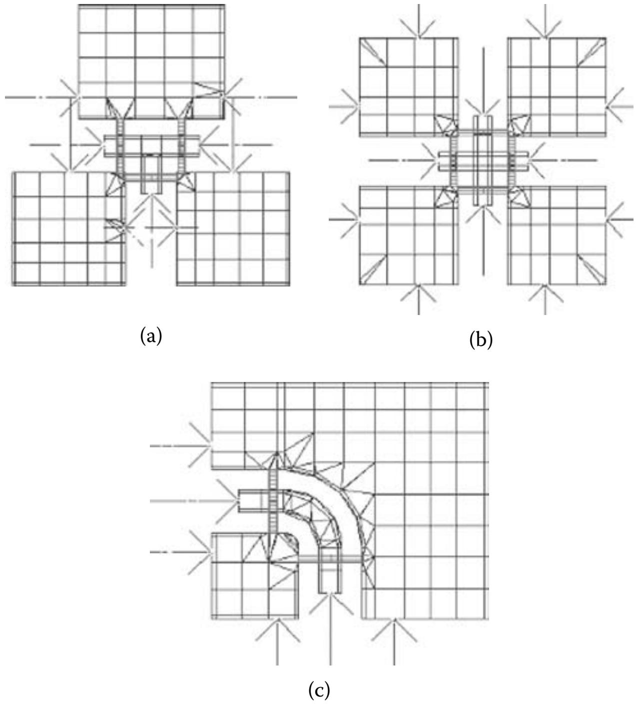

Figure 1.16 The CPW discontinuity patterns for EM analysis: (a) CPW "*Tee*," (b) CPW cross, and (c) CPW curve.

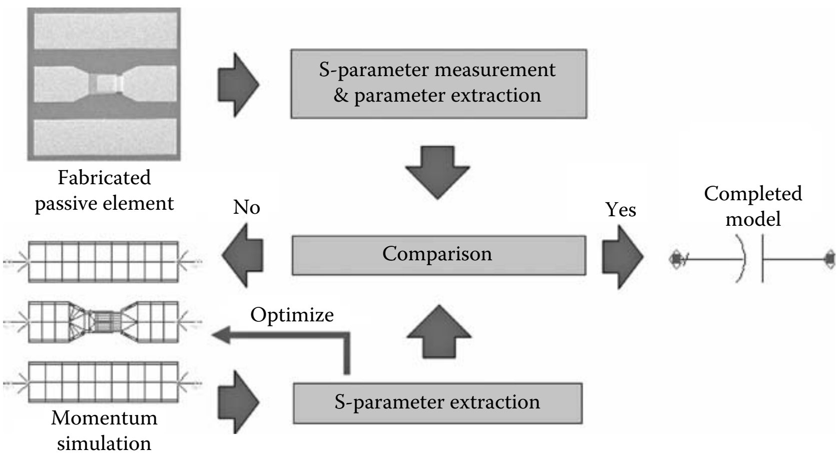

Figure 1.17 The extraction technology of the passive model.

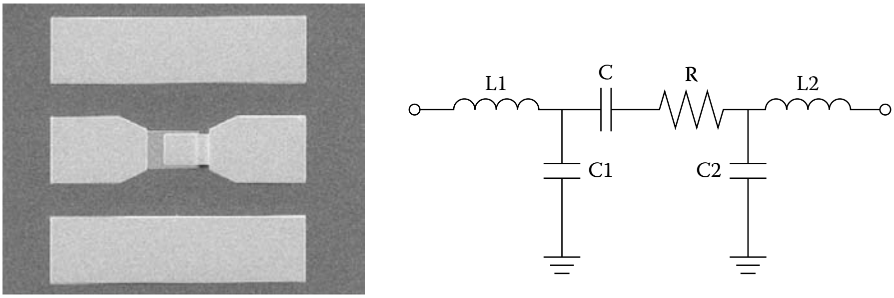

(a) (b)

Figure 1.18 The fabricated metal–insulator–metal (MIM) capacitor: (a) the micrograph of the MIM capacitor (capacitor size: 45 μm × 45μm), and (b) the equivalent circuit of the MIM capacitor.

Ti thin-film resistors were fabricated and modeled. Capacitors are used in MMICs for blocking and bypass purposes. Due to the high dielectric constant (r = 5.5–7.5) and breakdown field (> 106 V/cm), the Si3N4 is mostly preferred as a dielectric layer for MIM capacitors [21]. An Si3N4 film was deposited using the PECVD (plasma-enhanced chemical vapor deposition) system for the MIM capacitor. The connection between the top capacitor plate and adjacent metallization is an airbridge connection in order to avoid problems caused by edges and slopes. The SEM photography of the fabricated MIM capacitor is shown in Figure 1.18(a), and the applied lumped equivalent circuit is shown in Figure 1.18(b). Resistors are used in MMICs for several purposes including feedback, isolation, terminations, and voltage dividers (or self-biasing) in a bias network. Ti thin-film resistors allow precise control of resistance due to their small sheet resistances and have a large current capacity per unit width compared to resistors composed of the active GaAs material [22]. The SEM photography of the fabricated thin-film resistor is shown in Figure 1.19a, and the applied lumped equivalent circuit is shown in Figure 1.19b.

1.3.2 Design Technology of Millimeter-Wave Monolithic Circuits

In the field of a millimeter-wave monolithic circuit, more detailed design technologies are needed than for a microwave monolithic circuit. These needs can be met only by more accurate circuit simulation both for chip yield and electrical performance due to high frequency. Although an electromagnetic (EM) field analysis was used in millimeter wave, the efficient design method is required because of reduction of simulation time and stable design. The efficient design technology of a millimeter-wave monolithic

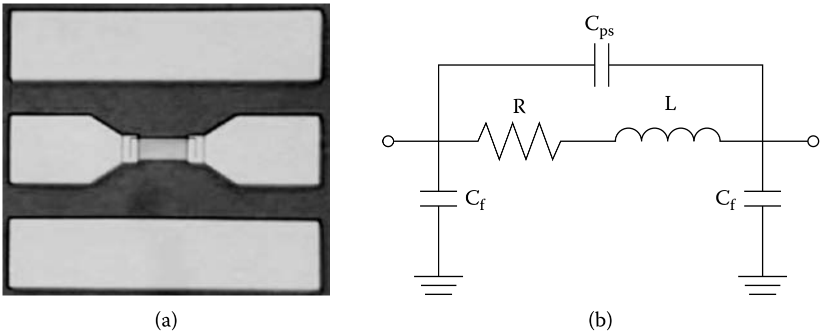

Figure 1.19 The fabricated Ti thin-film resistor: (a) the micrograph of the Ti thin-film resistor (length of 60 and width of 30) and (b) the equivalent circuit.

circuit is as follows: (1) perform modeling of active and passive devices, (2) determine the circuit topology, (3) perform initial design using circuit simulation based on CAD, (4) perform the preliminary circuit layout, (5) analyze using EM simulation of critical areas, (6) modify the circuit design and layout, (7) perform the resimulation for the modified circuit, (8) optimization through repeating phases (5–7). Figure 1.20 shows the design flow of a millimeter-wave monolithic circuit. Although design of a millimeter-wave monolithic circuit is similar to a microwave circuit design in phases 1–5, EM simulation and layout optimization are required due to the parasitic effect for accurate design. However, EM simulation requires a very long time and significant computing capacity, if the total MMIC pattern is

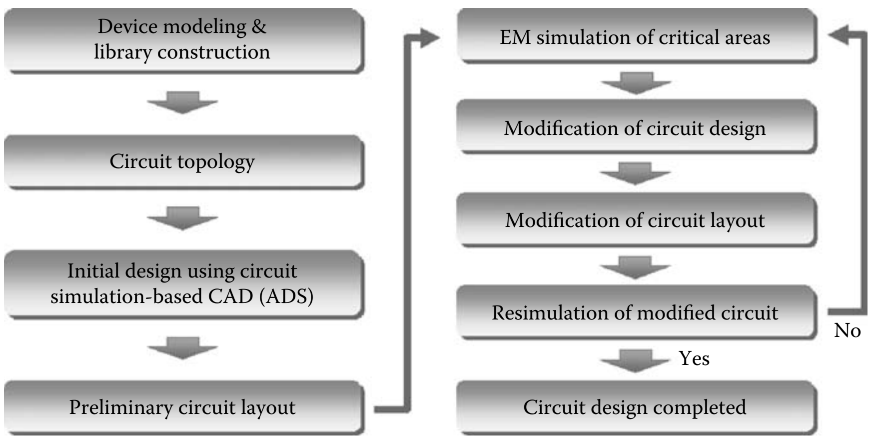

Figure 1.20 The design procedure of a millimeter-wave monolithic integrated circuit.

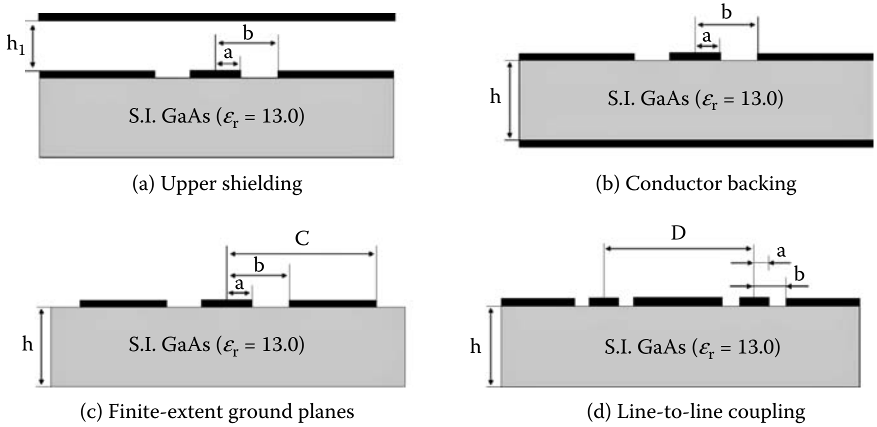

Figure 1.21 Parasitic effects of a CPW transmission line. (Taken from [23] IEEE 1987.)

simulated. Also, it is not easy for a designer to revise the circuit pattern through EM simulation of the total pattern. For design technology to solve this problem, analysis of a basic parasitic effect can be presented [23]. CPW offers several advantages over conventional microstrips for millimeter-wave monolithic circuit applications on GaAs substrates. But, CPW has parasitic effects such as upper shielding, conductor backing, lateral ground plane truncation, and line-to-line coupling. These parasitic effects change MMIC characteristics for various pattern shapes. Figure 1.21 explains the parasitic effects of a CPW transmission line. In millimeter-wave circuit design, some analysis concerning CPW lines on GaAs substrates can be used for the aim of practical design criteria. The effect of upper shielding basically results in a reduction of the line impedance. This is clearly seen in Figure 1.22, where the constant Zol curves are given in the plane a/b-h_1/b, while the substrate thickness was set to h/b = 1. Although the minimum cover height needed to avoid significant impedance lowering depends on the line impedance itself, as a conservative estimate the cover height should be at least hl = 4b. As expected, conductor-backed coplanar lines are slightly less sensitive than upper shielding coplanar waveguides for the same characteristic impedance. However, also for this case, the design criterion $h_1 > 3b$ is a conservative estimate. If the minimum substrate thickness needs to be independent of line impedance, then a rough estimate for a 50 line suggests $h/b > 3$ as a reasonable value (error with respect to $h/b \rightarrow \infty$ less than 2 percent). Figure 1.23 shows constant-impedance conductor-backed coplanar waveguide as a function of the shape ratio a/b. Finite ground-plane width leads to a slight increase of the line impedance with respect to the ideal case ($c \rightarrow \infty$, or $b/c \rightarrow 0$) as shown in Figure 1.24 ($h/b = 1$, C/b ranging from 1 to 3.33). In case

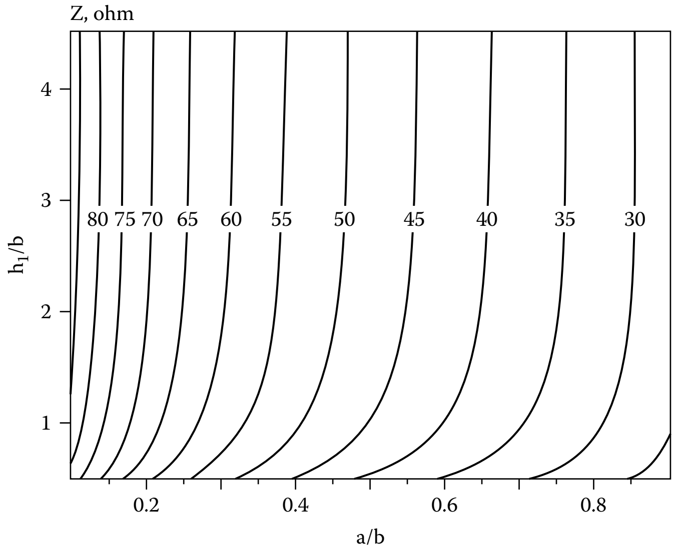

Figure 1.22 Constant impedance with upper shielding coplanar waveguide as a function of the shape ratio, a/b and the cover height, h_l/b, with substrate thickness h/b = 1 and GaAs substrate permittivity $\varepsilon_r = 13$. (Taken from [23] IEEE 1987.)

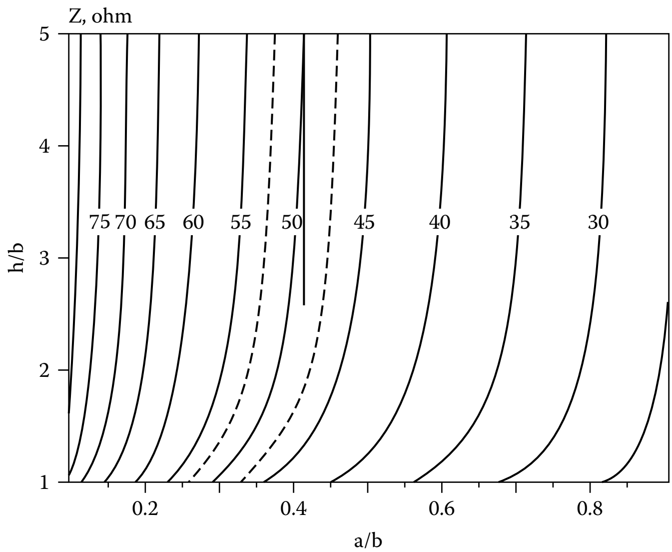

Figure 1.23 Constant-impedance conductor-backed coplanar waveguide without upper shielding as a function of the shape ratio, a/b, and the substrate thickness, h/b, with GaAs substrate permittivity $\varepsilon_r = 13$. (Taken from [23] IEEE 1987.)

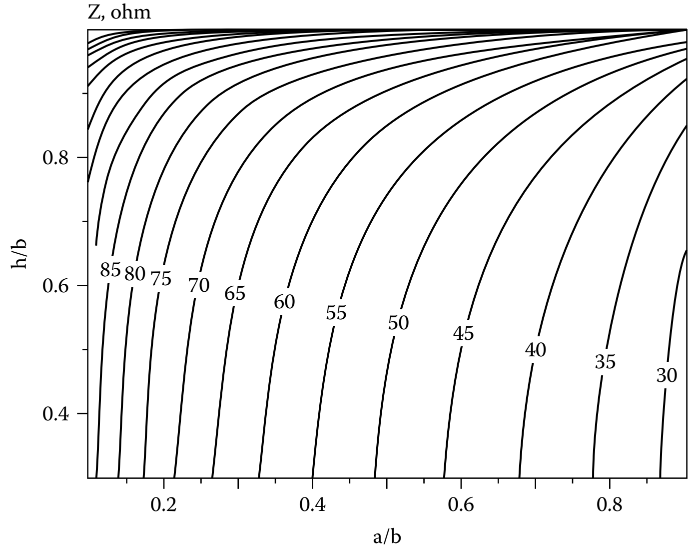

Figure 1.24 Constant-impedance coplanar waveguide with finite ground planes as a function of the shape ratio, a/b, and the inverse of the ground plane width, b/C, with substrate thickness h/b = 1 and GaAs substrate permittivity $\varepsilon_r = 13$. (Taken from [23] IEEE 1987.)

of very narrow lateral ground planes, the impedance is largely increased. As a conservative estimate, one should have C/b = 4 at least to ensure that the variation is negligible. As a last point, let us consider line-to-line coupling. A chart for evaluating this effect is shown in Figure 1.25. It can be seen that coupling weakly depends on the shape ratio a/b, whereas, as is obvious, it is strongly influenced by the line spacing D. From Figure 1.25, the minimum D needed to ensure coupling less than a given value can be obtained. As a conservative estimate of maximum coupling allowed, one can assume, for instance, the value of 40 dB, thereby requiring line spacing to be at least D/b = 7. Based on analysis of the CPW parasitic effect, we can expect a critical area with an electrical characteristic that is very different compared to the result of circuit-based simulation (ideal case). Figure 1.26 shows the preliminary layout of millimeter-wave amplifier and critical areas. Figure 1.27 is an EM simulation pattern for critical areas. The design example is a W-band MMIC amplifier employed in a two-stage structure with 70 μm $\times$ 2 MHEMTs. The matching circuit was designed using CPW transmission lines. The open stubs and transmission lines were used for matching circuits of input/output and the interstage. Also, the W-band MMIC amplifier was designed as a low Q-factor matching circuit structure to improve the broadband characteristic. The bias line was designed using $\lambda/4$ (at 100 GHz) short stub [24]. The initial designed W-band amplifier was

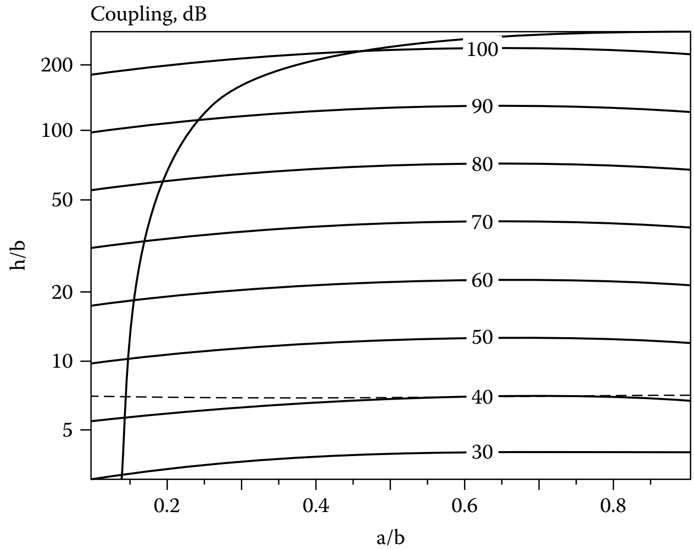

Figure 1.25 Constant-coupling curves for parallel coplanar lines on infinitely thick GaAs substrate ($\varepsilon_r = 13$) as a function of the shape ratio, a/b, and the normalized distance, D/b (log scale). (Taken from [23] IEEE 1987.)

optimized by the EM simulator (ADS Momentum™). When EM simulation was performed, only the critical area was optimized without total pattern simulation. Therefore, reduction of simulation time and efficient design are possible. Figure 1.28 shows comparison data of circuit-based simulation and EM simulation for the pattern in Figure 1.27. From analysis results, an

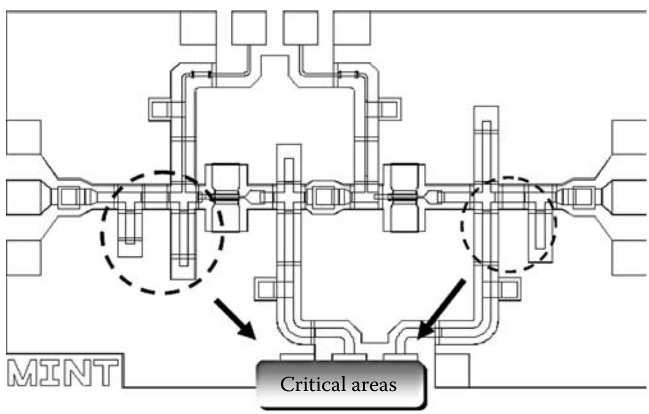

Figure 1.26 The preliminary layout of a W-band amplifier and critical areas.

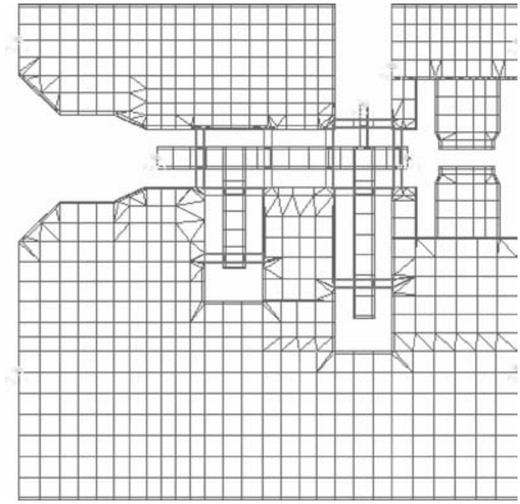

Figure 1.27 EM simulation pattern for critical areas.

apparent difference between circuit-based simulation and EM simulation of critical areas was obtained. The EM simulation exhibited higher impedance characteristics than circuit-based simulation (ideal case) due to parasitic effect (finite ground, line-to-line coupling). After the critical area was optimized, the completed amplifier circuit is shown in Figure 1.29. From the measured results, W-band MMIC amplifiers exhibit a broadband characteristic from the S21 gains of 11 ± 2 dB in a W-band frequency range of

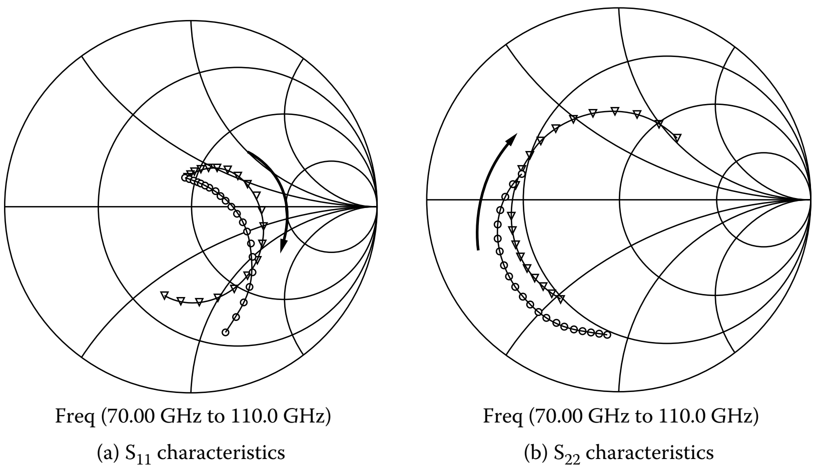

Figure 1.28 Comparison data of circuit-based simulation and EM simulation for critical areas (○: circuit-based simulation, ▽: EM simulation).

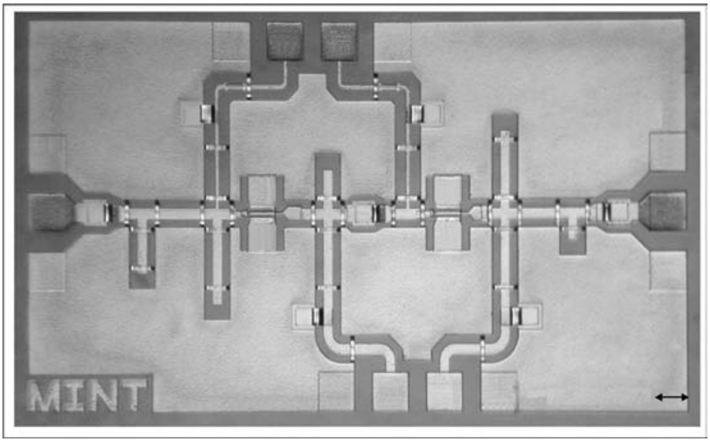

Figure 1.29 The fabricated MMIC W-band amplifier circuit (Millimeter-wave INnovation Technology Research Center (MINT) size: 1.8 × 1.0 mm^2. (Taken from [24] IEEE 2004.)

70–100 GHz with good return losses. Also, a good agreement was obtained with the S-parameter measurements over the entire frequency range from 70 to 100 GHz compared to the simulated data. As shown in Figure 1.30, this result demonstrates that the presented design technology is a reasonable and efficient method in millimeter-wave ranges.

1.3.3 Millimeter-Wave Monolithic Integrated Circuit for WLAN

1.3.3.1 60-GHz Band MMIC Amplifier and Oscillator

Amplifiers are the basic building block of a wireless LAN system and mainly perform an amplification of weak signal. Amplifiers can be classified as low noise, drive, power, and linear. Also, HEMT and HBT devices have been generally adopted for MMIC amplifiers of millimeter-wave WLAN and so on. Figure 1.31 shows the performance of the reported 60-GHz MMIC low-noise amplifier and power amplifier for millimeter-wave WLAN [25–37]. A low-noise amplifier shows an S21 gain of 14–22.8 dB and a noise figure of 2.2–5.8 dB in a frequency range of 58–62 GHz, respectively. In the case of the MMIC power amplifier, an S21 gain of 7.5–13.8 dB and output power of 23–26.8 dBm were reported. A V-band MMIC low noise amplifier chip for millimeter-wave WLAN is shown in Figure 1.32. The MMIC low-noise amplifier is a three-stage circuit structure and GaAs PHEMTs are used. Circuit performances show an S21 gain of a typical 20 dB and a noise figure of 4.2 dB in the 55–65 GHz frequency range. The measured results of

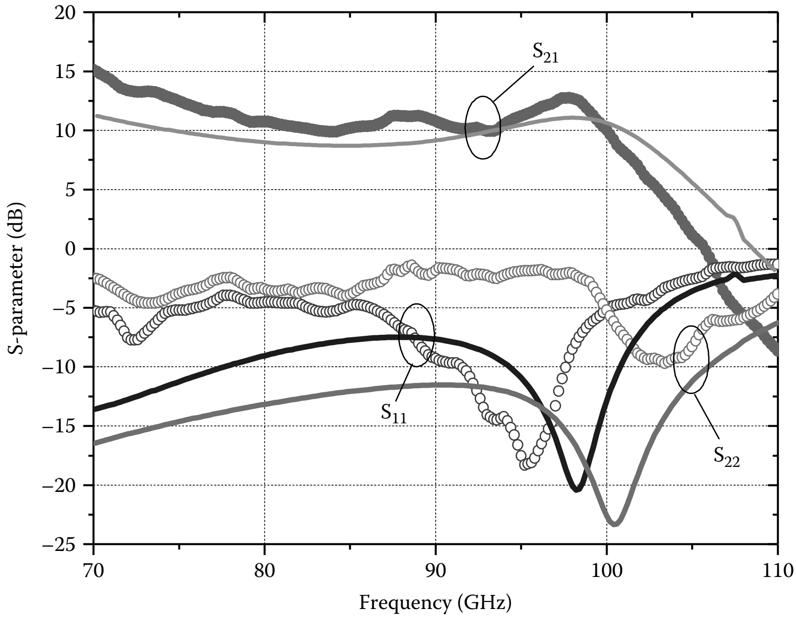

Figure 1.30 The simulated and measured results of the MMIC W-band amplifier circuit (o: measured data; —: simulated data). (Taken from [24] IEEE 2004.)

an MMIC low-noise amplifier are shown in Figure 1.33. This MMIC circuit can be used for the amplification block of a receiver in millimeter-wave WLAN. Oscillators are an essential block for millimeter-wave WLAN. Oscillators generate a millimeter-wave signal source using negative resistance. An ideal oscillator produces a pure sinusoidal carrier with fixed amplitude, frequency, and phase. Practical oscillators, however, generate carrier waveforms with parameters (oscillation frequency, output power) that may vary in time due to temperature changes and component characteristics. This phenomenon appears as phase and amplitude fluctuations at the oscillator output and will be of main concern in a wireless LAN system. Phase noise generation by the local oscillator at the receiver can significantly affect the performance of a wireless system. Figure 1.34 shows performance of the reported 60-GHz MMIC oscillator for millimeter-wave WLAN [38–41]. Oscillators show phase noise of −80 to −104 dBc/Hz and output power of 2.5–11.1 dBm in a frequency range of 56–62.5 GHz, respectively. Figure 1.35 is a photograph of the 60-GHz MMIC voltage-controlled oscillator (VCO), which was designed using GaAs PHEMTs. The VCO structure adopted an injection-locked VCO structure. CPW transmission lines and intrinsic gate capacitance of the HEMT are used for resonance at 60 GHz. To adjust the output frequency, a varactor diode of 280 width HEMT is used. A CPW

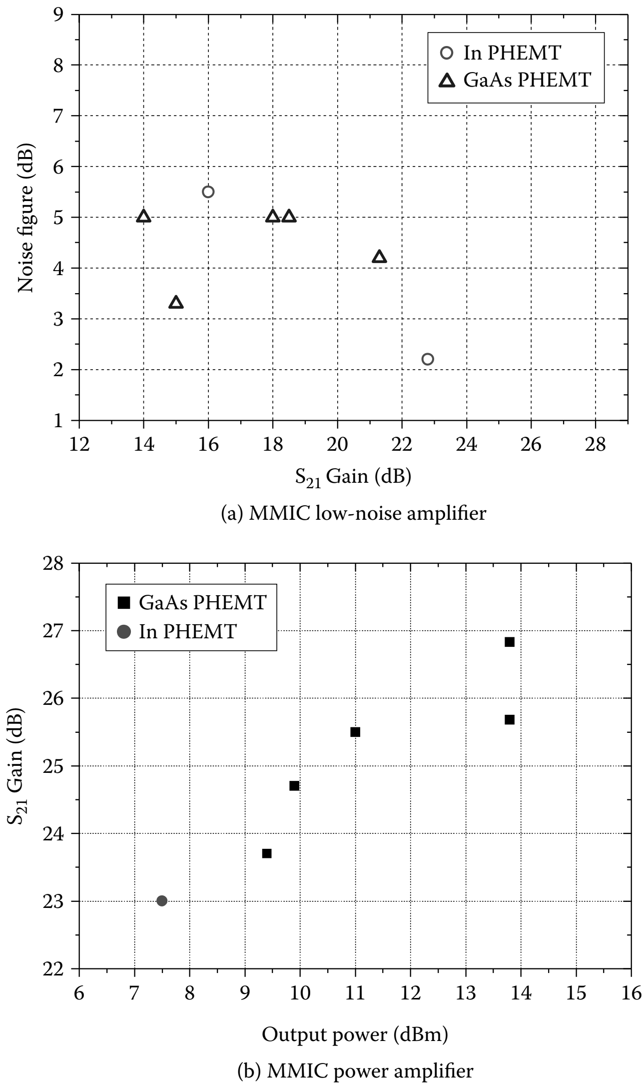

Figure 1.31 Performance of reported 60-GHz MMIC low-noise amplifier and power amplifier for millimeter-wave WLAN [25–37].

coupler is designed to inject the reference signal. The output phase of VCO is locked by the injected signal through the coupler. The major purpose of the buffer amplifier is to ensure proper matching of the oscillator output and isolation to the output port of VCO. Circuit performances show output power of typically 2.5 dBm and phase noise of 83 dBc/Hz (at 1 MHz offset) at 60 GHz oscillation frequency.

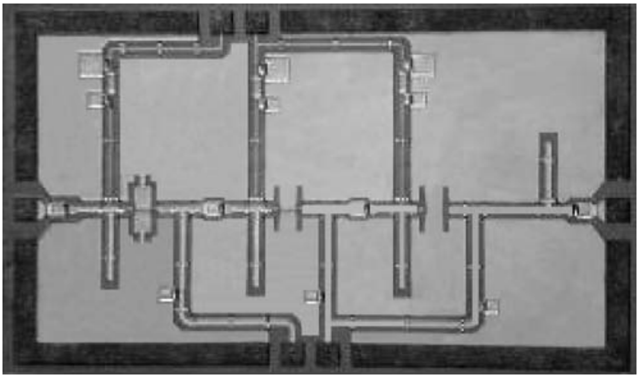

Figure 1.32 V-band MMIC low-noise amplifier for millimeter-wave wireless LAN (Millimeter-wave INnovation Technology Research Center (MINT); size: 2.6 × 1.5 μm^2) [25].

1.3.3.2 60-GHz Band MMIC Mixer

A mixer, or frequency converter, has the prime function of converting a signal from one frequency to another with minimum loss of the signal and minimum noise performance degradation. A mixer is one of the fundamental blocks of a wireless LAN system. A mixer faithfully preserves the amplitude and phase properties of the RF signal at the input. Therefore, signals can be translated into frequency without affecting their modulation properties. An ideal mixer multiplies the input signal by the sinusoidal signal generated by a local oscillator. This results in a mixed product that consists of higher and lower frequency components. Devices that exhibit

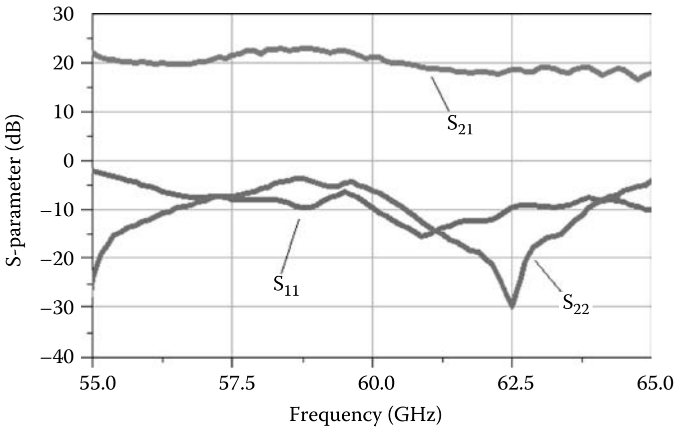

Figure 1.33 The measured results of a V-band MMIC low-noise amplifier [25].

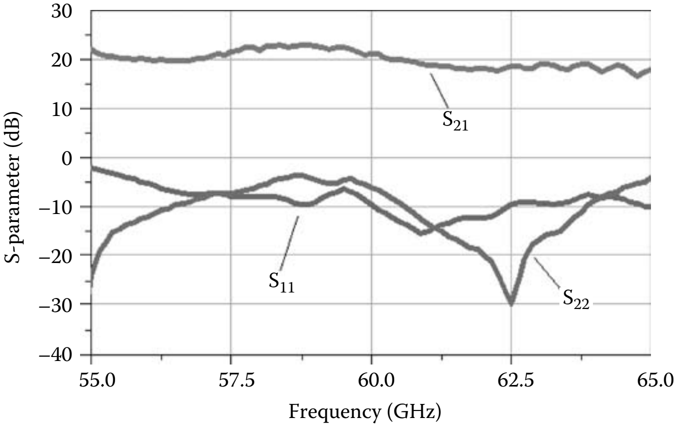

Figure 1.34 Performance of reported 60-GHz MMIC oscillator for millimeter-wave WLAN [38–41].

nonlinear or rectifying characteristics are good candidates for designing mixers. Diodes and HEMT devices are commonly used in the design of millimeter-wave mixers, because of their rectifying and nonlinear characteristics. Schottky barrier diodes have broad bandwidth and are low cost. Besides, diodes do not need DC bias to operate and have fast switching capability. On the other hand, HEMT or HBT devices have lower noise, better frequency response, and increased power handling ability. Also, HEMT and HBT devices are amenable to monolithic circuit integration. The

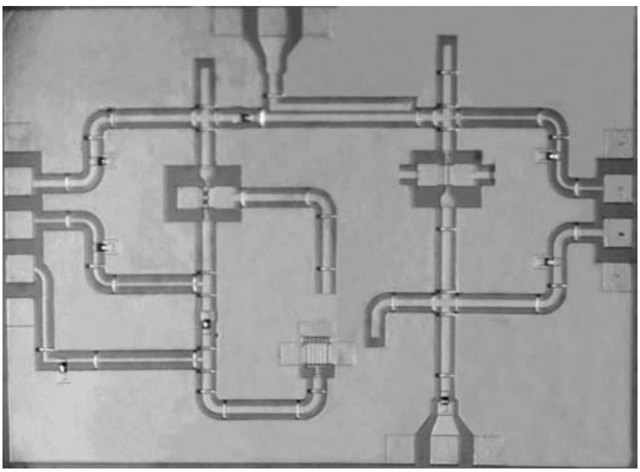

Figure 1.35 The 60-GHz MMIC voltage control oscillator (Millimeter-wave INnovation Technology Research Center (MINT); size: 2.2 × 1.6 μm^2).

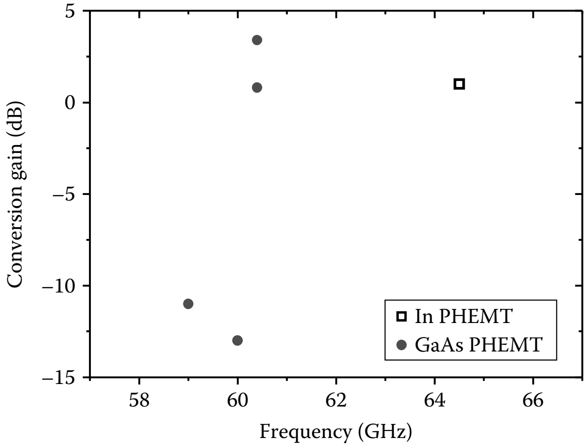

Figure 1.36 Performance of the reported 60-GHz MMIC mixer for millimeter-wave WLAN [42–46].

distortion caused by the inherent nonlinearities of the diodes is reduced in HEMT mixers. Figure 1.36 shows the performance of the reported 60-GHz MMIC mixer for a wireless LAN [42–46]. Conversion gains exhibit −13 to 3.4 dB in the frequency range of 59–64.5 GHz. Circuit structures have been studied in a single-ended diode mixer, balanced HEMT mixer, and balanced resistive mixer. A 60-GHz MMIC mixer chip for a millimeter-wave wireless LAN is shown in Figure 1.37. A circuit structure is a double-balanced

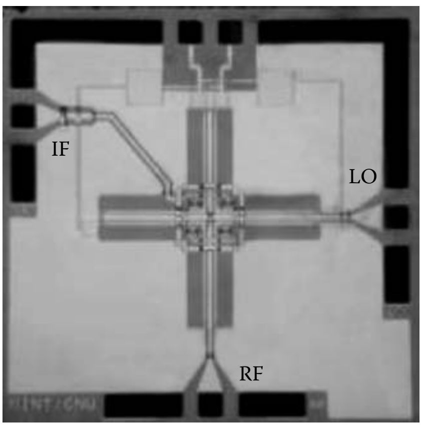

Figure 1.37 A 60-GHz MMIC mixer chip for millimeter-wave wireless LAN (Millimeter-wave INnovation Technology Research Center (MINT); size: 1.5 × 1.5 mm^2. (Taken from [45] IEEE 2005.)

star mixer and GaAs PHEMT is used. The novel star mixer is composed of gate-drain (GD)-connected PHEMT diodes where the gate-source junctions are reverse biased to pinch off. Due to the reverse bias, the mixing occurs mainly by the DS conductance rather than by the gate-source junction diode. Consequently, the conversion loss does not suffer degradation due to the hetero-junction diode. Besides, the DS conductance is not as highly nonlinear as the diode point of the structure; the star mixer has a simpler topology, whereas the resistive ring mixer requires three separate baluns. More wideband operation is possible with the removal of the IF (intermediate frequency) balun [45]. Circuit performances show conversion loss of a typical 13 dB and isolation of a 35 dB at all ports. This circuit can be used for up/down frequency converters in the millimeter-wave WLAN. Furthermore, a subharmonic mixer has been researched in millimeter-wave ranges because a stable local oscillator (LO) signal is indispensable to the mixers. However, it is practically difficult to fabricate a stable oscillator operating at 60 GHz or above. Thus, continuous research and development efforts on the subharmonic mixers have been made because they can utilize lower LO frequencies than the conventional mixers [47]. This approach allows the use of a local oscillator of a relatively low frequency because an LO frequency is located at some integer fraction (1/n) of the fundamental LO frequency. For this reason, the subharmonic mixers with antiparallel diode structure were evaluated at millimeter-wave frequencies [48]. Figure 1.38 shows the designed circuit schematic of the 60-GHz MMIC subharmonic mixer. In this

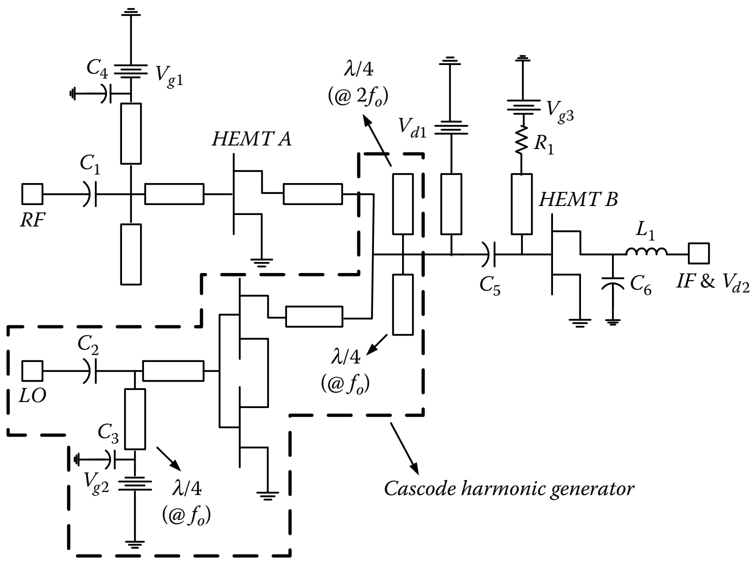

Figure 1.38 Circuit schematic of the 60-GHz MMIC subharmonic mixer. (Taken from [43] IEEE 2003.)

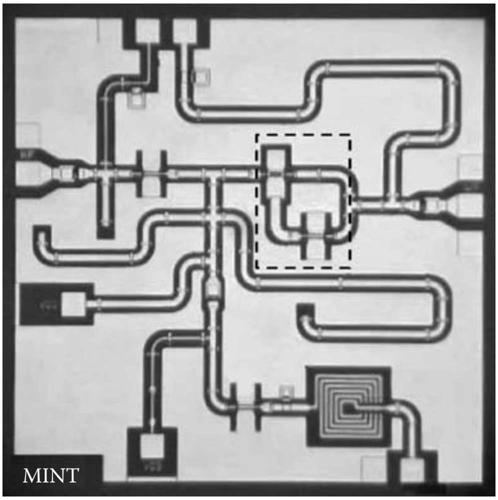

Figure 1.39 Micrograph of the fabricated MMIC subharmonic mixer (Millimeter-wave INnovation Technology Research Center (MINT); size: 1.9 × 1.8 mm^2; 2003 IEEE International Microwave Symposium; the cascode pair is shown in the dashed lines). (Taken from [43] IEEE 2003.)

work, a cascode harmonic generator is proposed to improve the conversion gain of the quadruple subharmonic mixer. The circuit of the subharmonic mixer was designed using the architecture of a gate mixer. An IF stage device (HEMT B) mixes the generated fourth harmonic signal and the RF signal. An RF stage device (HEMT A) not only amplifies the RF signal but also improves the LO–RF isolation due to the isolation characteristics of reverse direction. Matching circuits for the RF and the LO ports were designed using the CPW transmission lines. Figure 1.39 is a micrograph of the fabricated subharmonic mixer [43]. The measured results of the subharmonic mixer demonstrated that the conversion gain is 3.4 dB, which is a good conversion gain at the LO power of 13 dBm, as shown in Figure 1.40. Also, the conversion gain versus the LO input power was measured. The conversion gain is saturated at an LO input power level higher than 13 dBm, as shown in Figure 1.40. As shown in Figure 1.41, the fabricated subharmonic mixers show a good LO-to-IF isolation of −53.6 dB and LO-to-RF isolation of −46.2 dB at 14.5 GHz, respectively. The measurement results exhibited a high degree of isolation characteristics. The MMIC subharmonic mixer circuit provides high performance through the proposed cascode harmonic generator, and the cost of a wireless LAN system can be reduced because of utilization of a lower LO frequency than a conventional mixer. In addition, Figure 1.42 shows the circuit schematic and planar view micrograph of the fabricated 94-GHz MMIC resistive mixer chip using metamorphic

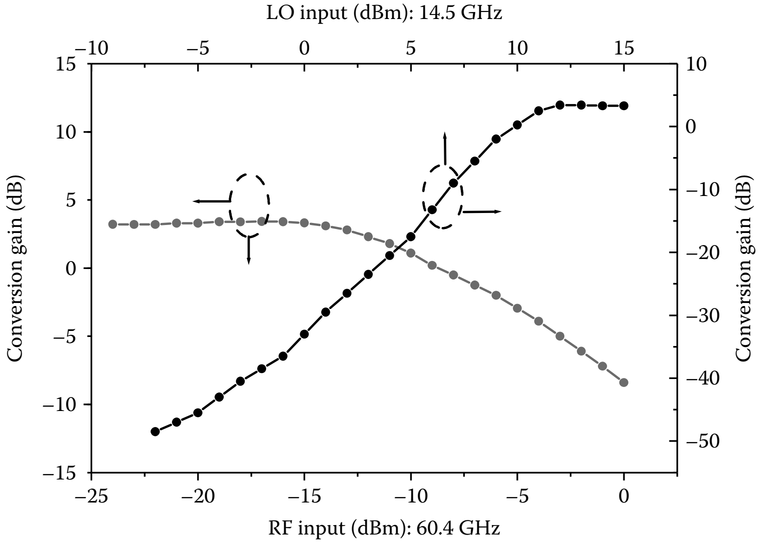

Figure 1.40 Conversion gain vs. RF input and LO input (RF frequency: 60.4 GHz; LO frequency: 14.5 GHz; IF frequency: 2.4 GHz). (Taken from [43] IEEE 2003.)

HEMTs [49]. Resistive mixers are widely used due to good conversion loss, low distortion, and no drain bias. Also, a frequency of 94 GHz has been actively researched as millimeter image sensor and FMCW (frequency modulated continuous wave) radar applications. However, the development of

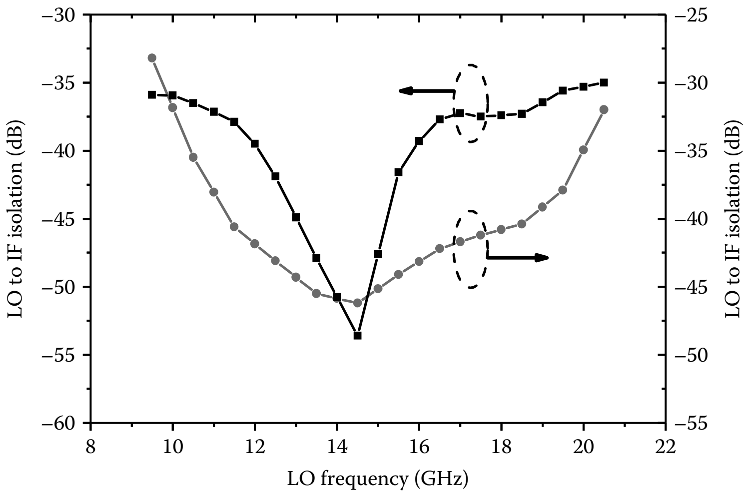

Figure 1.41 The measured results of isolation characteristics. (Taken from [43] IEEE 2003.)

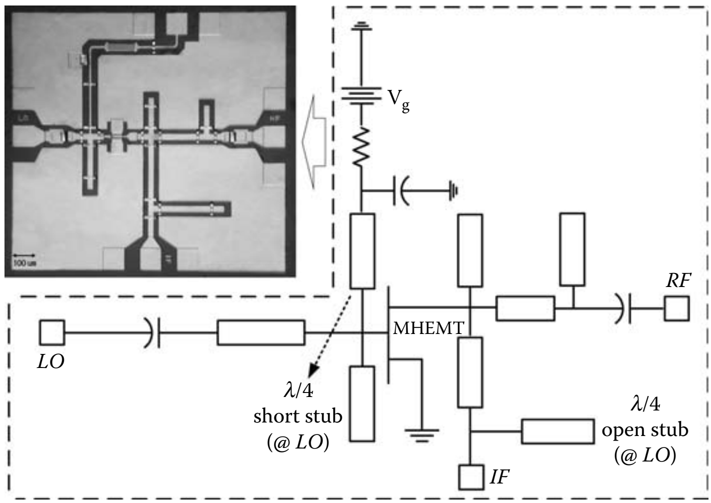

Figure 1.42 The circuit schematic and planar view micrograph of the fabricated 94-GHz MMIC resistive mixer (MINT), size: 1.2 × 1.1 μm^2. (Taken from [49] IEEE 2003.)

high-performance resistive mixers is difficult because of the limitations of the active device. Recently, GaAs-based metamorphic HEMTs (MHEMTs) adopted the low-cost GaAs substrates using the metamorphic buffers and higher indium mole fraction for the InGaAs channels than that of PHEMTs. Therefore, the MHEMTs materialize the same structure of InGaAs/InAlAs hetero-junction with the InP-based HEMTs and exhibit comparable RF performance for millimeter-wave applications [50]. The 94-GHz resistive mixer in this work was designed using MHEMTs for high performance. LO and RF matching circuits of the resistive mixer were implemented using coplanar waveguide transmission lines. A gate bias circuit was designed using a quarter-wavelength (4 at 94 GHz) short stub and a Ti thin-film resistor. A structure of a quarter-wavelength open stub was added at the IF stage for suppressing the LO signal at the IF port. The designed MMIC mixer was fabricated using the metamorphic HEMT-based MMIC process. Conversion loss of the mixer was measured with an applied RF signal of 94.075 GHz and an LO signal at 94.240 GHz. Conversion loss versus RF frequencies were obtained at an RF power of −20 dBm and LO power of 7 dBm. Figure 1.43 shows the simulated and measured conversion loss as a function of LO input power and RF frequencies. As shown in the plot, the resistive mixer exhibited a very low conversion loss of 8.2 dB at an LO power of 7 dBm. Compared to previously reported W-band (75–110 GHz) MMIC resistive mixers based on PHEMTs [51] or InP-based HEMTs [52], the MHEMT-based MMIC resistive mixer presented in this work has shown superior conversion loss.

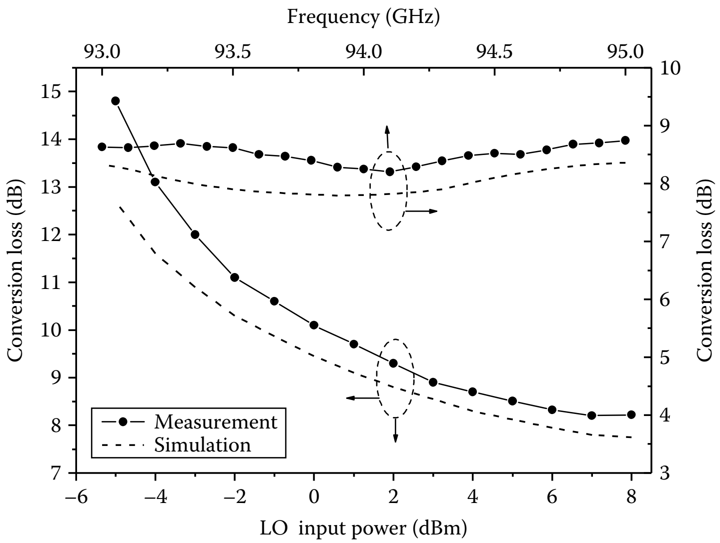

Figure 1.43 Conversion loss versus LO input power (at an LO frequency of 94.240 GHz, an RF frequency of 94.075 GHz, and an RF input power of −20 dBm) and RF frequencies (at an RF input power of −20 dBm and an LO input power of 7 dBm) measured for the MMIC resistive mixer. (Taken from [49] IEEE 2005.)

1.3.4 Fabrication Process of Millimeter-Wave Monolithic Integrated Circuits

There were few differences between the fabrication process for PHEMT-based MMICs and MHEMT-based MMICs, such as etching solution and metal thickness for ohmic contacts. However, a basic factor of fabrication is the same. In this chapter, we shall limit discussion of MHEMT-based MMICs. Fabrication processes for the MMIC were performed in the following sequence. First, mesa etching was done by the phosphoric acid-based etching solution. AuGe/Ni/Au for ohmic contacts were evaporated and annealed. After Ti metal evaporating for thin-film resistor, a 100-nm T-gate was patterned through a triple-layer resist pattern using electron beam lithography technology. Then, we performed a gate recess etching to control current of the devices. After the gate metal formation of Ti/Au, we performed the first-level metallization. And then, we deposited Si3N4 film for the passivation of MHEMTs and interlayer dielectric of the MIM (metal–insulator–metal) capacitor. After the RIE (reactive ion etching) process for opening the contact window, we finally performed the airbridge (second-level metallization) in order to connect between isolated electrodes.